

# LOCATIONS OF OPTICAL AND $\gamma$ -RAY EMITTING REGIONS IN THE JET OF PMN J2345-1555

YUN-GUO JIANG<sup>1</sup>, SHAO-MING HU<sup>1</sup>, XU CHEN<sup>1</sup>, XI SHAO<sup>1</sup>, QIU-HONG HUO<sup>2</sup>

<sup>1</sup>Shandong Provincial Key Laboratory of Optical Astronomy and Solar-Terrestrial Environment,  
 Institute of Space Sciences, Shandong University, Weihai, 264209, China ; jiangyg@sdu.edu.cn  
 and

<sup>2</sup> School of Space Science and Physics, Shandong University at Weihai, Weihai 264209, China

## ABSTRACT

We collect long term  $\gamma$ -ray, optical and radio 15 GHz light curves of the flat-spectrum radio quasar (FSRQ) object PMN J2345-1555. The correlation analyses between them are performed via the local cross-correlation function (LCCF). We found that all the optical  $V$ ,  $R$  band and the infrared  $J$  band are correlated with the radio 15 GHz with significance larger than  $3\sigma$ , and the lag times are  $-221.81^{+6.26}_{-6.72}$ ,  $-201.38^{+6.42}_{-6.02}$  and  $-192.27^{+8.26}_{-7.37}$  days, respectively. However, the  $\gamma$ -ray is correlated with the radio at only  $1.5\sigma$  significance level, and the lag time is  $-103.51^{+9.57}_{-8.69}$  days. The lag times enable us to derive that the optical  $V$  band and the  $\gamma$ -ray emitting regions are located at  $5.47 \pm 0.31$  and  $11.16 \pm 0.46$  parsec from the base of the jet, respectively. We present that time lags between different frequencies can be used as an alternative parameter to derive the core-shift measurement, and the magnetic field and particle density of jets can be derived by this method in a direct way. The variation of  $R - J$  color index shows a bluer when brighter trend. We also found that a  $3\sigma$  correlation between  $\delta V - \delta R$  and the radio light curve, which indicates that opacity plays an important role in the variation. As hinted from radio images, we proposed that the upstream and downstream emission component contributes the bluer and redder spectral index, respectively. Such spatial dependent spectral index model is complementary for the shock in jet model, and provides a new mechanism to explain various spectral index behaviors of blazars in a unified way.

**Keywords:** Blazar: individual(PMN J2345-1555) – galaxies:jets – radio continuum:galaxies

## 1. INTRODUCTION

In the unified model of active galactic nuclei (AGNs), blazars are of a special subclass whose relativistic jets point towards us, characterised by its violent variable in the whole electro-magnetic bands. The spectral energy distribution (SED) of blazars indicates two bumps, which are interpreted as the synchrotron and Compton processes, respectively. These emissions are believed to originate from jets, whose axial direction is near our line of sight. Except several nearby sources, blazars are point sources for optical telescopes and  $\gamma$ -ray detectors. Thus, the locations of the optical and  $\gamma$  regions are unsolved by observation directly. The multi-frequency data help to answer this question from different aspects. Some indirect methods have been proposed to study the location of  $\gamma$ -ray emission regions based on the rich data from *Fermi* large area telescope (LAT). By SED fitting with the one zone emission model, Kang et al. (2014) found that the best fitted parameters are obtained when the seed photons are from dust torus, which indicates that the  $\gamma$ -ray emission region is beyond the broad line region (BLR). Britto et al. (2016) studied one  $\gamma$ -ray outburst of 3C 454.3, and pointed out that gamma-ray emission region is on the edge of the BLR based on the minimal variable time scale. If this time scale is considered as the lower limit of the cooling time scale, the magnetic field can be derived via the synchrotron radiation process Yan et al. (2018). Respecting the scaling law, the location of the emission regions can be derived by matching the obtained value  $B_{\text{diss}}$  with results from the Very Long Baseline interferometry (VLBI) core-shift measurements. Using the similar method, Wu et al. (2018) first obtained the strength of the magnetic field by SED fitting, then derived locations of  $\gamma$ -ray emission region by the scaling law. However, the SED fitting process depends on free parameters, the coupling of them brings us a caution that best fitted results may deviate from the true physical values.

Impressive progresses have been made by several radio observation programs of AGNs in recent years Richards et al. (2011); Pushkarev et al. (2012); Fuhrmann et al. (2016); Lister et al. (2009). The high spatial resolution (milliarc-

second) of VLBI enables us to measure parameters of jets directly. The combination of VLBI radio images and the X-ray  $\gamma$ -ray light curves can provide a direct method to locate the emission regions. [Hodgson et al. \(2017\)](#) made long term VLBI observations for OJ 287,  $\gamma$ -ray data analysis combined with the radio images reveals that the  $\gamma$ -rays are radiated from the radio core regions, and strongly correlates with the jet structures in radio images. Also, [Algaba et al. \(2018\)](#) found that outbursts of  $\gamma$ -ray of 4C 38.41 can be traced back with the appearance of new knot structures in radio images. It is evident that gamma-ray originates from down stream regions in the jet. The discrete correlation function (DCF) analysis indicates that  $\gamma$ -ray leads to radio about 70 days, which corresponds to a 39 parsec distance between them. Time lags can be used in a direct method to locate the  $\gamma$ -ray emission regions [Fuhrmann et al. \(2014\)](#); [Max-Moerbeck et al. \(2014b\)](#). Using the discrete cross-correlation function (DCF) stacking technique, [Fuhrmann et al. \(2014\)](#) found significant correlations between  $\gamma$ -ray and multiple radio wavelengths in a sample with 54 blazars. The  $\gamma$ -ray emitting region is located upstream of 3 mm radio core regions. [Max-Moerbeck et al. \(2014b\)](#) studied the correlation between  $\gamma$ -ray and 15 GHz radio light curves by using the local cross-correlation function (LCCF). They found that four blazars in a sample with 41 sources have strong correlations with significance level beyond  $2.25\sigma$ . Compared to DCF, LCCF performs better in picking out the physical correlations [Max-Moerbeck et al. \(2014a\)](#). The location of the  $\gamma$ -ray emitting region can be calculated by the time lag analysis [Fuhrmann et al. \(2014\)](#); [Max-Moerbeck et al. \(2014b\)](#). Combined with jet parameters from VLBI results, this provides a direct method to derive the emitting regions.

In this work, we will study the location of optical and  $\gamma$ -ray emitting regions for target PMN J2345-1555 (B1950 name 2345-167) by the LCCF analysis. The target is of flat spectrum radio quasar (FSRQ) type with redshift  $z = 0.576$ . More than 8 years data in  $\gamma$ -ray, optical and radio bands are collected in Section 2. The details of LCCF and time lag analysis are presented in Section 3. We found significant correlations between optical  $V$ ,  $R$  and radio light curves. A time lag of 10 days was found between  $V$  and  $J$  bands, which indicates that the jet of target is very compact, and optical emission is not optically thin. The time resolved color index analysis reveals that this source becomes bluer when brighter. In Section 4, the theoretical frame is reviewed first. Then, we derive the location of emitting regions for optical and  $\gamma$ -rays for this target. The magnetic field strength and number density of radiative particles are derived according to the scaling law, which is a direct method to derive these jet parameters. The strong correlation between color index and the light curve gives us the hint that the optical emission region has a spectral distribution structure similar to that of radio. We propose that this provides a new mechanism to explain the variation of color index behaviors.

## 2. DATA COLLECTION AND REDUCTION

We collect the multiple wavelength data of the target from publicly available webs, including the Fermi LAT gamma-ray data [Atwood et al. \(2009\)](#), the optical photometry and polarization from Steward Observatory [Smith et al. \(2009\)](#), the 15 GHz radio data from Owens Valley Radio Observatory (OVRO) [Richards et al. \(2011\)](#).

**Fermi LAT data** More than seven years (from 2008 August 4 to 2017 February 25)  $\gamma$ -ray data of PMN J2345 – 1555 were retrieved from the public *Fermi Science Support Center* (FSSC). The downloaded data field is inside a region of interest (ROI) with  $15^\circ$  radius around the target, and the photon energy interval is between 0.3 and 300 GeV. The data analysis was performed by using the *Fermi ScienceTools* version v10r0p5. The instrument response function is the P8R2\_SOURCE\_V6. The Galactic and isotropic  $\gamma$ -ray background are counted by the gll\_iem\_v06 and P8R2\_SOURCE\_V6 file, respectively. The XML file uses the spectral model from the 3FGL catalog for all point sources in the field [Fermi LAT collaboration \(2015\)](#).

In the 3 FGL catalog, PMN J2345-1555 has the name ‘3 FGL J2345.2-1554’, which has a log-parabolic spectrum, the broken energy is taken to be 825.789 MeV. The *unbinned likelihood method* is used to analyze the eight years data. The temporal bin is 4 days, which produces the light curve of  $\gamma$ -ray with 782 points. We considered the photon energy in the range  $0.1 \sim 278.7$  GeV, and the energy bin is taken to divide the whole range into 6 parts with equal logarithmic length, which are labeled with **a**, **b**, **c**, **d**, **e** and **f**, respectively. This produces 6 light curves with different energy band in  $\gamma$ -ray, and will be used to produce the spectral fitting. The data points with error larger than the flux are kicked off to produce the light curves. We also set the threshold value of TS to be 2 for the spectral fitting. We found that the light curve of **b** band (i.e.,  $0.3 \sim 0.9$  GeV) have more valid points than that of **a** band. The maximal TS values in **b** band light curves reaches 349. The linear fittings are done on those time points with at least three valid fluxes (TS value larger than 2). The fitting function is given by

$$\log F_\gamma(E) = \alpha \log E + A_0. \quad (1)$$

Finally, we obtain a light curve of the  $\alpha$  with 164 points and read out its corresponding flux.

**Photometry and polarization data** The optical and the polarization data are downloaded from the public Steward observatory database <sup>1</sup>, which is performed to support the *Fermi* missions [Smith et al. \(2009\)](#). The optical data were obtained by the 2.3 m Bok Telescope and the 1.54 m Kuiper Telescope. The polarization measurement was performed by the SPOL spectropolarimeter [Schmidt et al. \(1992\)](#). Due to various reasons like the lunar phase, the bad weather, and competition from other programs for telescope time, the data was unevenly sampled. The polarization degree (PD) and polarization angle (PA) on the web have been calibrated. In this work, both  $\delta V$  and  $\delta R$  relative magnitude of the target source from 2011 November 7 to 2017 July 1 are available. The optical  $R$  and near-infrared  $J$  band data from SMARTS were also downloaded <sup>2</sup>. The data is observed from 2011 Nov. 08 to 2015 Jun. 26, which has already been calibrated [Bonning et al. \(2012\)](#). Although it covers a shorter time duration than the Steward data, the more intensive sample rate makes it suitable for correlation analysis. The optical finding chart of the target presents the  $R$  band magnitude of the comparing star '6' to be 16.04, this comparing star is named as 'A' in Steward's finding chart. We use this comparing star to calibrate the  $R$  magnitudes of the Steward data. The light curves for  $R$  and  $J$  band fluxes are plotted in Fig.(2). The  $R - J$  color index are plotted in Fig. (9). The correlation between the magnitude and CI is studied in the next section.

For the PA, there is the  $n\pi$ -ambiguity problem, so the continuous rotation of the PA can not be directly presented by the available data [Marscher et al. \(2008\)](#); [Kiehlmann et al. \(2016\)](#). We diminish the  $n\pi$ -ambiguity by using the method proposed by [Kiehlmann et al. \(2016\)](#). The code is written according to the formula

$$\chi_{i,\text{adj}} = \chi_i - n \cdot 180^\circ, \quad n = \text{round} \left( \frac{\chi_i - \chi_{i-1}}{180^\circ} \right). \quad (2)$$

Since the original PA data covers almost six years, several observation gaps exist for the PA time series due to the observation cycles. The change speed of PA is rapid for this target, and a hand-operated  $\pm 180^\circ$  shift for one observation cycle is allowed. However, we did not adjust the data by hand to keep the smoothness of the adjustment. The adjusted PA value are in the range  $-600^\circ \sim 180^\circ$ . The adjusted PA light curve is presented in Fig. (1).

**Radio 15 GHz data** This research has made use of data from the OVRO 40-m monitoring program ([Richards et al. 2011](#)). The measurements are not evenly sampled and are performed about twice per week. In this study, the observed data are collected from 2010 november 9 to 2017 September 8, during which 570 measurements are available. The data has already been calibrated, and light curve is presented in Figure (1).

### 3. CORRELATION AND SPECTRA ANALYSIS

In order to investigate the location of the emission regions in jets and the emission mechanism, we perform the correlation analysis between different light curves and study the time-resolved spectra in both the  $\gamma$ -ray and optical bands.

#### 3.1. Correlation Analysis

The correlations for light curves at different bands are important to reveal the emission mechanism of blazars. For unevenly sampled light curves, the discrete correlation function (DCF) is suitable to calculate correlations [Edelson & Krolick \(1988\)](#). However, DCF can also predict spurious peaked lags due to the intrinsic properties of the light curves [Max-Moerbeck et al. \(2014a\)](#). Besides, the value of DCF can exceed the  $[-1, 1]$  range due to the few valid points at certain lags. Welsh invented the localized cross-correlation function (LCCF) to constrain the range of correlations [Welsh \(1999\)](#). It is shown that LCCF is also efficient than the DCF in picking up the physical signal. Thus, we take use the LCCF to calculate correlations between light curves at different bands. In order to estimate the significance of the time lag, the Monte Carlo (MC) method is applied to estimate the significance of the correlation. The MC procedure follows [Max-Moerbeck et al. \(2014a\)](#). First,  $10^4$  artificial radio light curves are simulated by the method given in [Timmer and Koenig \(1995\)](#) (TK95). The spectral slope of power-density spectrum (PDS) is fixed at  $\beta = 2$ . Then LCCF between these artificial light curves and the observed light curve are calculated. At each lag bin, one has  $10^4$  correlation coefficients, and 0.01% precision can be achieved for the significance estimation. It has been verified that the distribution of these values is of the normal type. Then the  $1\sigma$ ,  $2\sigma$  and  $3\sigma$  significant levels corresponding to the 68.26%, 95.45% and 99.73% chance probabilities are obtained.

One needs to determine the time lag and its  $1\sigma$  error range, if the significance level of the correlation peak is high. Two kinds of time lags can be obtained from the LCCF plots, i.e., the location of the peak of LCCF  $\tau_p$  and the centroid

<sup>1</sup> <http://james.as.arizona.edu/~psmith/Fermi/>

<sup>2</sup> <http://www.astro.yale.edu/smarts/glast/home.php>

around the peak of the LCCF  $\tau_c$ . The centroid lag are calculated by counting the lags whose correlation values are above half of the peak correlation. The  $1\sigma$  error ranges of both  $\tau_p$  and  $\tau_c$  are calculated via the model independent Monte Carlo method [Perterson et al. \(1998\)](#). We develop the code which combines the flux randomization (FR) and the random subset selection (RSS) processes [Lasson \(2012\)](#).  $10^4$  time simulations are performed to obtain the distribution for both  $\tau_p$  and  $\tau_c$ . In Figure (3), histograms of  $\tau_c$  and  $\tau_p$  for both the optical V-band and CI versus radio are plotted.

Based on these codes, the LCCF analysis are performed between different light curves. We found that all the optical  $V$ ,  $R$  and  $J$  bands lead to the 15 GHz radio  $-221.81^{+6.26}_{-6.72}$ ,  $-201.38^{+6.42}_{-6.02}$  and  $-192.27^{+8.26}_{-7.37}$  days ( $\tau_c$ ), respectively. We also found that  $\delta V - \delta R$  CI is strongly correlated with the radio light curve. All the peaks of LCCF are beyond the  $3\sigma$  significance level, see Figure (4). It is evident that  $V$  band leads to  $J$  band  $-10.01^{+3.08}_{-3.22}$  ( $1\sigma$ ) days, see Figure(5). The time lag between the optical and the near-infrared indicates that this source is very compact, and even the optical emission is not optically thin. One can refer that the synchrotron peak in SED may be higher than the infrared frequencies, which is unusual for FSRQ. The  $\gamma$ -ray leads to the 15 GHz  $-103.51^{+9.57}_{-8.69}$  days, but the significance is only  $\sim 1.5\sigma$ , see Figure(6). We did not find time lags between the internal  $\gamma$ -ray bands, i.e. **a**, **b**, **c** and **d**. There is also no significant correlation between the optical and the  $\gamma$ -ray. In Tab. 3.1, we summarize the lag times (both  $\tau_p$  and  $\tau_c$ ) relative to the 15 GHz for other curves.

**Table 1.** Time lag and distances relative for the radio light curve

	$\gamma$ -ray	$V$ band	$R$ band	$J$ band
$t_c$ (days)	$-103.51^{+9.57}_{-8.69}$	$-221.81^{+6.26}_{-6.72}$	$-201.38^{+6.42}_{-6.02}$	$-192.27^{+8.26}_{-7.37}$
$t_p$ (days)	$-106^{+28}_{-0}$	$-210^{+4}_{-16}$	$-208^{+23}_{-12}$	$-187^{+2}_{-19}$

NOTE—Here  $t_c$  and  $t_p$  denote the centroid and peak time lags (in unit of days), respectively.

In Figure (7), the LCCF of the adjusted polarization angle (PA) and the polarization degree (PD) versus radio are plotted. The correlation between adjusted PA and radio is below the  $1\sigma$  level. Various strategies have been tried to adjust the PA, no significant correlation is found. The time sample of polarization is not good enough, and there is no concrete method to eliminate the  $n - \pi$  ambiguity in principle. From the PD versus radio analysis, one can find  $2\sigma$  correlation signals. However, the significance lines are narrow compared to the PA case. This may be caused by the moderate variation of PD light curves. At the optical lag time  $-200$  days, the PD is anti-correlated with the radio fluxes, which indicates that the PD decreases when the optical flux increases. Such phenomenon may be due to that the optical emission region includes more disordered magnetic fields in the flare state.

### 3.2. Variation of spectral index

The light curves of the spectral index and the flux can be analysed by the LCCF analysis, which offers us a time-dependent method to study the variation behavior. To investigate the time-independent CI behaviors, we plot the  $\delta V - \delta R$  versus  $\delta V$  in the left panel of Figure (8). It is evident that the  $V$  band flux is strongly variable, since the  $\delta V$  covers from  $-3$  to  $1$ , while the  $\delta V - \delta R$  CI is in the range  $-0.4$  to  $-0.1$ . We make use of the linear fitting  $y = a + bx$  to study their relations. For  $\delta V < -2$ , the green (solid) line has a slope  $0.047$ , and its Pearson's  $r$  value is  $0.642$ . This indicates a bluer-when-brighter trend for the flare state. For  $\delta V > -2$ , the  $(b, r)$  of the cyan (dash dot) line is  $(-0.004, -0.106)$ . This means that the CI is almost independent of the flux variation in non-active states. In the right panel of Figure (8), the negative correlation coefficients around the zero lag time indicate that  $\delta V - \delta R$  and  $\delta V$  behave inversely in variation. This is a redder-when-brighter trend. The value of LCCF is in fact the Spearman coefficient, which also presents an correlation analysis of the two light curves. Around zero, the average value of LCCF is  $-0.2$ , which indicates that the redder-when-brighter trend is not significant.

In Figure (9), the  $R - J$  versus  $R$  and LCCF between them are plotted in the left and right panel, respectively. In the left panel, the Pearson's coefficient of the linear fitting (blue solid line) is  $0.433$ , and the slope of it is  $0.201$ . This is a bluer-when-brighter trend. The better time sample of the data leads to a more significant correlation, and no evident time lag was found. This indicates that the  $R$  mag decreases as  $R - J$  decreases, which is also the bluer-when-brighter trend. The peak of LCCF is  $0.624$ . Compared with the behavior of the  $\delta V - \delta R$ , we found that this two color index

varies differently, which is unusual since  $V$ ,  $R$  and  $J$  frequencies are so close. In Figure (2), it is evident that the time sample from SMARTS is much intensive than that from Steward, and the latter misses many  $R$  band flares. This indicates that time sample are important for the LCCF analysis.

The spectral indices of  $\gamma$ -ray versus  $b$  band  $\gamma$ -ray fluxes are plotted in the left panel of Figure(10). We found that the spectral index shrinks to the range  $-0.6 \sim -1.1$  at high flux states, and is much more scattering at low flux states. Such phenomena have also been reported by Lico et al. (2014) for Mrk 421 and Algaba et al. (2018) for 4C 38.41. It is notable that the spectra indices of three targets tend to approach certain values when the flux reaches its maximum, see Figure 6 in Lico et al. (2014) and Figure 5 in Algaba et al. (2018). One possible reason is that the spectral index of the gamma-ray reflects that of the electron directly in the Compton scattering process. The electron spectrum is mainly determined by the acceleration mechanism in the most active state. The three targets all are of FSRQs, but have different values for the spectral index at their maximal fluxes.

There is a caveat that the value of the spectral index may depend on the adopted time bin. We used the four days bin to do the analysis, while Lico et al. (2014) and Algaba et al. (2018) used the standard week bin data. Since we set the critical TS value to be 2, and require at least three fluxes at one time bin to perform the linear spectral fitting. The shorter time bin tends to produce the harder spectra if the variable time scale of  $\gamma$ -ray is less than the bin. If the tendency is not due to the data selection effects, one can use them to constrain the emission mechanism for the  $\gamma$ -ray. For the shock acceleration, the typical spectral slope is  $p \approx 2.2 \sim 2.3$  Achterberg et al. (2001). For the magnetic reconnection, the resulted spectrum of electrons can be very hard, and an extreme  $p \approx 1$  can be achieved Guo et al. (2015). However, no conclusive results can be given here.

In the right panel of Figure (10), we present the LCCF of the  $\gamma$ -ray fluxes and the spectral indices (blue solid line) and the LCCF of the spectral index itself (red dash line). We found that the gamma-ray flux variation leads to the spectral index about 20 days. The significance of such correlation is weak due to the sparse time series of the spectral index. The lag of the spectral index may be due to that cooling time scale is shorter than the acceleration time scale, and the higher energy electrons need more acceleration time to be produced. However, we also perform the LCCF analysis between different energy bands of  $\gamma$ -rays, no evident time lags are found. Therefore, the intrinsic reason can be excluded. The reason to explain the time lag phenomenon is that the spectral index decreases as the flux increases. In correlation analysis, the lag time mostly denotes the time interval between the peak in two light curves. Due to the index behavior, the peak of the flux light curve will correspond to the valley of the index light curve. Thus, the lag time is roughly equal to the time interval between the peak and valley in the index light curve. The self-correlation of the spectral index light curve indicates that the correlation coefficient changes sign at about 20 days. This naturally explains the 20 days lag between flux and the spectral index. Therefore, the time-dependent spectra analysis can reveal variability behavior. The time-independent analysis shown in the left panel covers such behavior.

#### 4. DISCUSSION

The strong correlations between the optical, near-infrared and radio indicate that the jet in PMN J2345-1555 is very compact. Due to the opacity, the photosphere positions at sequent frequencies will systematically shifts towards the downstream of the jet, this leads to the core-shift phenomenon in the milliarcsecond resolution VLBI observations Konigl (1981); Lobanov (1998); Hirotani (2005). Kudryavtseva et al. (2011) proposed that time lags between different frequencies can play the same role as the core shift since they are both related to the projected distance in the sky. By using the time lags, many jet properties can be studied. In the following, we will present a theoretical frame. Based on which, many variation phenomena can be explained. Then, we explore the location of the optical emission regions, and derive many aspects of the jet.

##### 4.1. Theoretical frame

The convention in this part mostly follows Hirotani (2005) (H05 hereafter). First one takes the assumption of the scaling law that the magnetic field and the proper number density of electrons follow  $B^* = B_1 r^{-m}$  and  $N^* = N_1 r^{-n}$ , where  $r$  is in parsec units which represents the distance in jet,  $B_1$  and  $N_1$  refers to corresponding values at 1 pc.  $r_1 = 1\text{pc}$  is in convention. The flux intensity for the uniform slab of plasma in the jet is given by Hirotani (2005)

$$S_\nu = \frac{\pi}{4} \left( \frac{\theta_d}{\text{rad}} \right)^2 \left( \frac{\delta}{1+z} \right)^{1/2} A \nu^{5/2} (1 - e^{-\langle \tau_\nu \rangle}), \quad (3)$$

where  $A = (3/2)^{-\alpha} \frac{e\alpha(\alpha)}{cC(\alpha)} (\frac{e}{2\pi m_e c})^{-3/2} B^{-1/2}$ , and  $\langle \tau_\nu \rangle$  is the geometrical averaged optical depth at  $\nu$ . Here  $\alpha$  is a typical spectral index defined as  $S_\nu \propto \nu^\alpha$ . For flux in the optical thin region, we assume  $\alpha < 0$ . The flux density here is valid both in the optically thin and thick regions, one can check that the spectral index for  $\nu$  is in the range

$(5/2, \alpha)$ . The averaged optical depth can be expressed by  $\langle \tau_\nu \rangle = \alpha_\nu R_{\text{eff}}$ , where  $\alpha_\nu$  and  $R_{\text{eff}}$  stands for the synchrotron self-absorption (SSA) coefficient and the effective length along the line of sight in the observer frame, respectively. In geometry, one has  $R_{\text{eff}} = fr_\perp / \sin \varphi$  and  $r_\perp = r_1 r \sin \theta$ , where  $\theta$  is the jet opening angle,  $\varphi$  is the viewing angle, and  $f$  is a dimensionless geometrical factor from integration. For the slab geometry, one can take  $f = 1$  and for others one usually has  $f < 1$ .  $\alpha_\nu / \sin \varphi$  is Lorentz invariant, The absorption coefficient  $\alpha_\nu^*$  is given by

$$\alpha_\nu^* = C(\alpha) \frac{e^2}{m_e c} \frac{-2\alpha}{\gamma_{\min}^{2\alpha}} \left( \frac{e}{2\pi m_e c} \right)^\epsilon N^* B^\epsilon \nu^{*(-1-\epsilon)}. \quad (4)$$

where  $\epsilon \equiv 3/2 - \alpha$  and  $C(\alpha)$  originates from SSA counting (details are referred to Table 1 in H05). Considering the scaling law, the averaged optical depth is given by

$$\langle \tau_\nu \rangle = \Sigma(\alpha) N_1 B_1^\epsilon \left( \frac{\delta}{1+z} \right)^\epsilon r^{1-n-m\epsilon} \nu^{-1-\epsilon}, \quad (5)$$

where  $\Sigma(\alpha) \equiv fr_1 C(\alpha) \frac{-2\alpha}{\gamma_{\min}^{2\alpha}} \frac{e^2}{m_e c} \left( \frac{e}{2\pi m_e c} \right)^\epsilon \frac{\sin \theta}{\sin \varphi}$ . Here  $\delta$  is the Doppler factor and  $z$  is the redshift. Setting  $\langle \tau_\nu \rangle = 1$ , one obtains the distance between the core position for observed frequency  $\nu$  and the base of the jet, i.e.,

$$r_{\text{core}}(\nu) = \Sigma(\alpha)^{\frac{1-k_b}{k_r}} \left( \frac{\delta}{1+z} \right)^{\frac{k_b}{k_r}} N_1^{\frac{1-k_b}{k_r}} B_1^{\frac{k_b}{k_r}} \nu^{-\frac{1}{k_r}}, \quad (6)$$

where indices are defined by

$$k_b \equiv \frac{3-2\alpha}{5-2\alpha}, \quad (7)$$

$$k_r \equiv \frac{(3-2\alpha)m+2n-2}{5-2\alpha}. \quad (8)$$

$r_{\text{core}}(\nu)$  denotes the photosphere position of frequency  $\nu$  in the jet. Assuming there are two different frequencies  $\nu_1$  and  $\nu_2$ , one can obtain the photosphere distance between them by two kinds of observations. One is the high spatial resolved VLBI observation, another is the time lag analysis between well sampled time series. Here we present the relation between them via the projected distance  $\Delta r_{\text{proj}}$ , i.e.,

$$\begin{aligned} \Delta r_{\text{proj}} &= [r_{\text{core}}(\nu_2) - r_{\text{core}}(\nu_1)] \sin \varphi \\ &= \frac{\Omega_{r\nu}}{r_1} \left( \nu_2^{-1/k_r} - \nu_1^{-1/k_r} \right) \\ &= \frac{\beta_{\text{app}} c \Delta t_{\nu_1 \nu_2}^{\text{obs}}}{1+z}, \end{aligned} \quad (9)$$

where  $\Omega_{r\nu}$ ,  $\beta_{\text{app}}$  and  $\Delta t_{\nu_1 \nu_2}^{\text{obs}}$  are the core-position offset, the apparent velocity of the jet and the time lag between light curves of  $\nu_1$  and  $\nu_2$  in observer frame, respectively. Note that  $\beta_{\text{app}} \equiv \beta \sin \varphi (1 - \beta \cos \varphi)^{-1}$  can also be expressed as  $\beta_{\text{app}} = \Gamma \delta \beta \sin \varphi$ , where  $\Gamma$  is the Lorentz factor and  $\delta = \Gamma^{-1} (1 - \beta \cos \varphi)^{-1}$  is the Doppler factor (Pushkarev et al. (2010); Max-Moerbeck et al. (2014a,b)). These parameters can be measured by the VLBI observation (Hovatta et al. (2009); Pushkarev et al. (2010, 2012)). The core-position offset  $\Omega_{r\nu}$  is defined as (Lobanov (1998))

$$\Omega_{r\nu} \equiv 4.85 \times 10^{-9} \frac{\Delta r_{\nu_1 \nu_2} D_L}{(1+z)^2} \frac{\nu_1^{1/k_r} \nu_2^{1/k_r}}{\nu_2^{1/k_r} - \nu_1^{1/k_r}} \text{pc} \cdot \text{GHz}, \quad (10)$$

where  $\Delta r_{\nu_1 \nu_2}$  is units of milliarcseconds, and can be measured by the core shift in VLBI radio images. In Eq.(9), it is evident that  $\Omega_{r\nu}$  corresponds to the lag time  $\Delta t_{\nu_1 \nu_2}^{\text{obs}}$  in the following

$$\Omega_{r\nu} = \frac{\beta_{\text{app}} c \Delta t_{\nu_1 \nu_2}^{\text{obs}}}{1+z} \frac{\nu_1^{1/k_r} \nu_2^{1/k_r}}{\nu_2^{1/k_r} - \nu_1^{1/k_r}} \text{pc} \cdot \text{GHz}, \quad (11)$$

which enable us to measure the core-position offset via the lag time  $\Delta t_{\nu_1 \nu_2}^{\text{obs}}$ .

From Eqs.(6) and (9), it is possible to estimate  $B_1$  and  $N_1$  via multiple frequencies core-shift or time lag observations in principle. The index  $k_r$  can be obtained by the core-shift measurement  $\Delta r_{\nu_1 \nu_2}$  (O'Sullivan & Gabuzda (2009)), or by time lags  $\Delta t_{\nu_1 \nu_2}^{\text{obs}}$  in multiple radio band observations (Fuhrmann et al. (2014)). Under the assumption that the magnetic field energy density is equal to the particle, and jet is optically thick due to SSA,  $k_r$  is roughly equal to 1.

In the equipartition condition, the spectral index  $\alpha$  is  $-0.5$ . Then, the magnetic field and electron number density at 1 pc can be calculated by [Hirovani \(2005\)](#); [O'Sullivan & Gabuzda \(2009\)](#); [Zamaninasab et al. \(2014\)](#)

$$\begin{aligned} B_1 &\simeq 0.025 \left[ \frac{\sigma_{\text{rel}} \Omega_{r\nu}^3 (1+z)^2}{\theta \sin^2 \varphi \delta^2} \right]^{1/4}, \\ N_1 &\simeq 3.3 \left[ \frac{\sigma_{\text{rel}} \Omega_{r\nu}^3 (1+z)^2}{\gamma_{\text{min}}^2 \theta \sin^2 \varphi \delta^2} \right]^{1/2}, \end{aligned} \quad (12)$$

where  $\gamma_{\text{min}}$  is the minimal electron Lorentz factor,  $\sigma_{\text{rel}}$  is the ratio between the energy density of magnetic field and that of non-thermal particles which is set to be 1. Substituting Eq. (11) into (12), one can obtain these two parameters from the time lag result directly, i.e.,

$$\begin{aligned} B_1 &\simeq 0.025 \left[ \frac{\sigma_{\text{rel}} (\beta_{\text{app}} c \Delta t_{\nu_1 \nu_2}^{\text{obs}})^3}{(1+z) \theta \sin^2 \varphi \delta^2} \frac{\nu_1^3 \nu_2^3}{(\nu_2 - \nu_1)^3} \right]^{1/4}, \\ N_1 &\simeq 3.3 \left[ \frac{\sigma_{\text{rel}} (\beta_{\text{app}} c \Delta t_{\nu_1 \nu_2}^{\text{obs}})^3}{\gamma_{\text{min}}^2 (1+z) \theta \sin^2 \varphi \delta^2} \frac{\nu_1^3 \nu_2^3}{(\nu_2 - \nu_1)^3} \right]^{1/2}. \end{aligned} \quad (13)$$

The validity of these equations are based on the assumption that photosphere emission is dominant at both  $\nu_1$  and  $\nu_2$ .

#### 4.2. Location of emission regions

For this source, the jet parameters are measured by the MOJAVE projects [Pushkarev et al. \(2012\)](#) with the IAU source name '2345-167'. Its redshift  $z$ , apparent velocity  $\beta_{\text{app}}$ , core shift measure  $\Omega_{r\nu}$  and absolute distance  $r_{\text{core}}(15\text{GHz})$  are 0.576, 13.45, 18.44 pc · GHz and 16.18 pc, respectively. The lower limit of Lorentz factor  $\Gamma_{\text{min}}$  can be estimated by  $\Gamma_{\text{min}} = \sqrt{1 + \beta_{\text{app}}^2}$ , which is 13.49 (roughly the same with  $\beta_{\text{app}}$ ) for our target. The viewing angle  $\varphi$  can be solved analytically by

$$\cos \varphi = \frac{\beta_{\text{app}}^2 - \sqrt{\beta_{\text{app}}^2 (\beta^2 - 1) + \beta^2}}{\beta (1 + \beta_{\text{app}}^2)}. \quad (14)$$

For  $\beta_{\text{app}} = 13.45$ , the parameter in the square root must be positive, which sets a strict lower limit for  $\beta$ , i.e.,  $\beta \geq 0.9972$  or  $\Gamma \geq 14.15$ . We conclude that  $\beta \approx 1$  is a reasonable assumption for approximation. Substituting  $\beta_{\text{app}} = 13.45$  into  $\approx (\beta_{\text{app}}^2 - 1)/(\beta_{\text{app}}^2 + 1)$ , one obtains that  $\varphi \approx 8.5^\circ$ . Another crude method to estimate the viewing angle is  $\varphi \approx \sin^{-1}(1/\Gamma_{\text{min}}) \approx 4.25^\circ$  [O'Sullivan & Gabuzda \(2009\)](#), which is about half of the previous one. The latter method behaves good only in the statistical manner [Cohen et al. \(2007\)](#). We will take  $\varphi \approx 8.5^\circ$  in the follows. The Doppler factor can be estimated by  $\delta = \Gamma^{-1}(1 - \beta \cos \varphi)^{-1} \approx 5$ . [Pushkarev et al. \(2009\)](#) have presented that the apparent opening angle  $\theta_{\text{app}} \approx 15.8^\circ$ . The intrinsic opening angle is  $\theta_{\text{intr}} = \theta_{\text{app}} \sin \varphi \approx 2.3^\circ$ .

The most natural way to explain the time lag between optical and radio is that the optical emission region is upstream and the radio emission region is downstream of the jet. The distance between them is given by [Pushkarev et al. \(2010\)](#); [Fuhrmann et al. \(2014\)](#)

$$r_{\text{core}}(\nu_2) - r_{\text{core}}(\nu_1) = \frac{\Gamma D \beta c \Delta t_{\nu_1 \nu_2}^{\text{obs}}}{1+z} = \frac{\beta_{\text{app}} c \Delta t_{\nu_1 \nu_2}^{\text{obs}}}{(1+z) \sin \varphi}. \quad (15)$$

Substituting  $\beta_{\text{app}} = 13.45$  and  $\Delta t_{V-15\text{GHz}}^{\text{obs}} = -221.81_{-6.72}^{+6.26}$  into equation (15), we obtained the distance between the emission region of the optical V band and that of 15 GHz, i.e.,

$$\Delta r_{V-15\text{GHz}} \approx \frac{(\beta_{\text{app}}^2 + 1) c \Delta t_{V-15\text{GHz}}^{\text{obs}}}{2(1+z)} = 10.71 \pm 0.31 \text{ pc} \quad (16)$$

The VLBI core-shift measurements presents  $r_{15\text{GHz}} = 16.18 \text{ pc}$  [Pushkarev et al. \(2012\)](#). The distance between the optical emission region and the central engine is thus  $r_V = 5.47 \pm 0.31 \text{ pc}$ . At this position of the jet, the magnetic field and the electron number density are 0.16 Gauss and  $137/\gamma_{\text{min}}$ , respectively. With  $t_{V-15\text{GHz}}^{\text{obs}}$ , the core-shift offset  $\Omega_{r\nu}$  is  $\simeq 23.86 \text{ pc} \cdot \text{GHz}$ , which is larger than the reported 18.44.

The typical size of the BLR region is less than 2 pc, so the optical emission region of PMN J2345 – 1555 is most probably beyond the BLR region. [Ghisellini et al. \(2013\)](#) have presented that the fluxes of the infrared, ultraviolet (UV) and  $\gamma$ -ray band changed quasi-simultaneously during one flare period, which indicated these emissions are located at one position of the jet. The SED showed that the peak frequency moves toward the bluer part when

the flare occurs, and such behavior is interpreted as the emission region moves from within the BLR to the outside. However, it is an indirect method to determine the jet parameters by SED fitting, and fitting is not unique in principle. Although the change of the emission region can not be excluded by our analysis, our results tends to claim that most of the optical emissions arise from certain positions in the jet, which is outside of the BLR region.

By the same procedure, one can also obtain that the  $\gamma$ -ray emission region is upstream of the radio emission region, but downstream of the optical emission region. The distance between the gamma and radio emission region is

$$\Delta r_{\gamma-15\text{GHz}} \approx 5.02 \pm 0.46 \text{ pc}. \quad (17)$$

The significance level of this correlation is less than  $2\sigma$ , which indicates that the particle population which produces the  $\gamma$ -ray affects the downstream, but the behavior of the radio emission only partly affected by the  $\gamma$ -ray regime. The optical activity play the dominant role in determining the radio behaviors. The correlation analysis also indicates that there is no correlation signal between the optical and  $\gamma$ -ray. Combing with the relative distance analysis, it is possible that the  $\gamma$ -ray is produced by the outflow from the optical region colliding with the some inner stationary components in the jet. These components may be of the slowing down matter of the flow or the transverse drift matter from other regions. [Hodgson et al. \(2017\)](#) used the global VLBI network to monitor the OJ 287 for a long period. They found that the  $\gamma$ -ray emission region is located at downstream of jet coincident with the radio core region. The flare behavior of the  $\gamma$ -ray is strongly correlated with the radio flare and the variable structure in the radio images. [Algaba et al. \(2018\)](#) made the multi-wavelength correlation analysis on 4C 38.41. The  $\gamma$ -ray leads to the radio about 70 days, and they found the flare of the  $\gamma$ -ray is correlated to the radio knot behavior. This means the  $\gamma$ -rays are produced in the downstream of the jet. However, the optical emission also leads to the radio at  $2\sigma$  level, and seems to lead the  $\gamma$ -ray without the error bar. Our analysis on PMN J2345-1555 have the similar location order sequence, but the significance of optical and radio correlation is larger than that of the  $\gamma$  and radio correlation. Since the optical and the  $\gamma$ -ray are produced at different emission regions,  $\gamma$ -ray is most probably produced by the external Compton (EC) scattering of the seed photons from torus. [Kang et al. \(2014\)](#) used the SED fitting technique to study the  $\gamma$ -ray emission region for a sample of bright blazars, and concluded that the seed photons most probably comes from the dust torus. However, the SED fitting is an indirect method to determine the emission region. Our time lag analysis is a more direct method, and the similar results are obtained.

The time lags measurement enables us to study the magnetic field and the number density of electrons.  $B_1$  and  $N_1$  can also be evaluated by Eq.(12). With the calculated parameters above, we obtain  $B_1 \approx 0.88$  Gauss and  $N_1 \approx 4095/\gamma_{\min}$ . The value of  $B_1$  approaches the reported 0.9 Gauss in [Pushkarev et al. \(2012\)](#). In the optical emission region, the magnetic field and the electron number density are calculated to be  $B \approx 0.16$  Gauss and  $N^* \approx 135/\gamma_{\min} \text{ cm}^{-3}$ , respectively. For synchrotron radiation, one can estimate the observed peak flux from the formula as follow

$$F_{\nu, \max} = (1+z)\delta^3 \left( \frac{N_T^* P_{\nu, \max}}{4\pi d_L^2} \right), \quad (18)$$

where  $P_{\nu, \max} = m_e c^2 \sigma_T \Gamma B / 3q_e$  is the synchrotron peak spectral power, and  $N_T^* = \frac{4\pi}{3} R^3 N^*$  is the total lepton number [Sari et al. \(1998\)](#).  $R = c\delta t_{\text{var}}$  can be estimated by the self-correlation LCCF of the optical light curves, where  $\delta t_{\text{var}} = 48 \pm 2$  days is the lag where the value of LCCF changes sign. For  $z = 0.576$ , one can obtains the luminosity distance  $d_L \approx 1.3 \times 10^{28} \text{ cm}$ . With  $\delta = 5$  and  $z = 0.576$ , one obtains that  $F_{\nu} \approx \gamma_{\min}^{-1} 10$  Jansky for optical  $R$  band. The observed flux of  $R$  band can be as high as 25 Jansky, see Figure 2. Since  $F_{\nu} \propto \delta^3$ , the discrepancy between observation and theory can be easily explained if  $\delta$  varies moderately [Chatterjee et al. \(2012\)](#).

With the known parameters, one can easily obtains the maximal luminosity in optical  $R$  band, i.e.,  $L_{\text{Opt}} \approx 2.5 \times 10^{50}$  ergs. Then the luminosity of the accretion disk can be estimated by the empirical relation [Zamaninasab et al. \(2014\)](#)

$$\log_{10} L_{\text{acc}} = 12.32 \pm 0.32 + 0.78 \pm 0.01 \log_{10} L_{\text{H}\beta} \quad (19)$$

where  $L_{\text{H}\beta} = 4\pi d_L^2 F_{\text{H}\beta}$ .  $\text{H}\beta$  line flux of this target is measured by [Jackson & Brown \(1991\)](#), i.e.,  $\lambda F_{\lambda} = 3.4 \times 10^{-11} \text{ ergs}^{-1} \text{ cm}^{-2}$ . By Equation (19), one obtains  $L_{\text{acc}} = 10^{47.47 \pm 0.79} \text{ ergs}^{-1}$ . Therefore, the accretion disk contributes little for the total observed flux, and the jet radiation is dominant for this target.

#### 4.3. Variable mechanism

The photosphere emission model can also help us to study the spectral lag phenomenon. Combing with the scaling law, the flux density is given by

$$S_{\nu} = \Xi(\alpha) \left( \frac{\theta_d}{\text{rad}} \right)^2 \left( \frac{\delta}{1+z} \right)^{1/2} B_1^{-1/2} r^{m/2} \nu^{5/2} (1 - e^{-\langle \tau_{\nu} \rangle}) \quad (20)$$

where  $\Xi(\alpha) \equiv \frac{\pi}{4} \left(\frac{3}{2}\right)^{-\alpha} \frac{e}{c} \frac{a(\alpha)}{C(\alpha)} \left(\frac{e}{2\pi m_e c}\right)^{-3/2}$ . The spectral index at frequency  $\nu$  can be derived by

$$\alpha_\nu = \frac{d \log S_\nu}{d \log \nu} = \frac{5}{2} + \left(\alpha - \frac{5}{2}\right) \frac{\langle \tau_\nu \rangle e^{-\langle \tau_\nu \rangle}}{1 - e^{-\langle \tau_\nu \rangle}}. \quad (21)$$

where  $\alpha$  is the spectral index of the synchrotron radiation at the optically thin region. In order to discuss how the opacity and flux varies along the jet, we set  $m = 1, n = 2$  and  $\alpha = -1.5$ . In the upstream jet, the optical depth can be much larger than one. One has  $S_\nu \propto r^{1/2} \nu^{5/2}$ . However, the optical depth decreases dramatically along the jet, i.e.,  $\langle \tau_\nu \rangle \propto r^{-4}$ . The photosphere occurs for  $\langle \tau \rangle = 1$ , one can derive that  $\alpha_\nu \approx 1 + 0.58\alpha$ . For  $\alpha = -1.5$ , one has  $\alpha_\nu \approx 0.13$ , which roughly agrees with the observed flat spectral index in the core region [Potter & Cotter \(2012\)](#). When the optical depth becomes much less than one, one has  $S_\nu \propto r^{-7/2} \nu^{-3/2}$ . Equation (20) reflects that the optical depth plays a key role in curvature effects of the spectrum. From Equation (20) and (21), it is evident that both  $S_\nu$  and  $\alpha_\nu$  strongly depends on  $\langle \tau \rangle$ . The variation of  $\langle \tau \rangle$  of the emission region will leads to the variation of both  $S_\nu$  and  $\alpha_\nu$ , which can explain the observed  $3\sigma$  correlation between  $\delta V - \delta R$  and the radio light curve. Since  $\langle \tau \rangle \propto r^{1-n-m\epsilon}$ , the analysis here presents us an  $r$ -dependent model of  $\alpha_\nu$  and  $S_\nu$ . In Figure(12), their dependence on  $r$  are plotted without considering physical parameters and units. The flux  $S_\nu$  is plotted according to the formula  $S_\nu = 10r^{1/2}(1 - e^{-5r^{-4}})$ . The plots of  $S_\nu$  and  $\alpha_\nu$  agree well with both the flux contours and spectral index maps in VLBI radio images, see Figure 1 and 6 in [O'Sullivan & Gabuzda \(2009\)](#).

The  $r$ -dependent spectral index model also provides us a new mechanism to explain both the bluer-when-brighter in the flare state and redder-when-brighter in the quiescent state. The upstream and the downstream emission regions can be considered as two components contributed to the observed total flux. When an emission blob propagates along the jet, the upstream will become bright first. This component will contribute a relative bluer spectral index to the total flux, which produces a bluer-when-brighter trend. When the emission blob occurs in the down stream, its kinetic energy has been dissipated previously in the up stream, and the transferred radiative energy is limited, which corresponds to a quiescent state. The spectral index tends to be smaller in the optically thin region. Besides, it can also accounts for the observed time lags at multi-frequencies. An animation made by 15 GHz VLBI images is presented by [Lister et al. \(2016\)](#). This target has a bright core, and the extended knot structures are evident for short time periods. Due to the strong correlation, one can infer that the optical image is very similar to that of the radio. This can explain the observed bluer-when-brighter trend of  $R - J$  and the doubtful redder-when-brighter trend of  $\delta V - \delta R$  for our target.

The other two reasons for the variation of color index includes the contamination from disk or other regions and the evolution of electron spectrum. [Villata et al. \(2006\)](#) found a redder-when-brighter trend during flares for 3C 454.3, which is explained by the presence of a luminous accretion disk, and the accretion process contributes significantly in the bluer band. The increase of the synchrotron radiation will enhance the flux in the redder band. Such trend has also been found for the target PKS 1502+106 [Ikejiri et al. \(2011\)](#). Also, for 3C 454.3, a color index saturation phenomena was also reported by [Tachibana and Kawai \(2015\)](#). Both the accretion disk model and the  $r$ -dependent spectral index model can explain the saturation, since there is a limit for the spectral index of the synchrotron emission. The disk contamination model is also of a two component model.

The bluer-when-brighter trend can be explained by the particle acceleration in relativistic jet [Kirk et al. \(1998\)](#). [Kirk et al. \(1998\)](#) presented that the spectrum becomes harder when the flux increases, under the assumption that the acceleration time scale of electron is shorter than that the cooling time scale. The bluer band is radiated by the high energy electrons quickly accumulated in a short time. Thus, the spectra becomes hard when the flux rises, and become soft when the flux decays. This produces the bluer-when-brighter trend. A spectral lag relative to the flux will be observed in the same time. When the acceleration and cooling time scales are almost the same, one observes that the spectra soften when the flux rises, and harden when the flux decays. A redder-when-brighter trend is produced. Thus, the shock in jet model can also produce two inverse trends of variation, which does not conflict with the  $r$ -dependent spectral index model. These two models are different aspects of the jet emission, one concentrates on the intrinsic energy injection of plasma, the other concentrates on the geometry structure of the total emission regions. Since the strong shock occurs when the relativistic blob collides with stationary components in jet, which most probably happens in the upstream jet. The kinetic energy is dissipated via radiation. When it arrives the downstream, the non-relativistic collisions most probably happens. The opacity condition plays a role in the shock in jet model, but is not manifested by references. The shock in jet model predicts the  $\gamma$ -ray emission via the synchrotron self-Compton process(SSC), which will be strongly correlated with the optical emission. The absence of this correlation in our target may be due to that the optical depth of  $\gamma$ -ray is larger than one. The shock in jet model can not be excluded by this phenomenon. Thus, both acceleration and opacity condition are important to study the jet emission processes.

## 5. CONCLUSION

In this work, we performed the LCCF analysis to study correlations between 8 years light curves of the  $\gamma$ -ray, optical bands and 15GHz radio. The obtained time delays enable us to study locations of the  $\gamma$ -ray and optical emission regions. The time-resolved spectra analysis is performed to investigate the spectral behaviors at different wavelengths. We present a unified theoretical frame to explain the observed light curve and spectral behavior. The principle conclusions are given in the follow

- Based on the more than  $3\sigma$  significance signals, the optical  $V$  band,  $R$  band and the infrared  $J$  band leads to the 15 GHz radio with  $-221.81^{+6.26}_{-6.72}$ ,  $-201.38^{+6.42}_{-6.02}$  and  $-192.27^{+8.26}_{-7.37}$  days, respectively. Combined with the apparent velocity from the VLBI results, the  $V$  band emission region locates at  $5.47 \pm 0.31$  pc away from the base of the jet. The sequence of the lag days at three frequencies indicates that the jet is very compact, even the optical emission regions are not optically thin. A less than  $2\sigma$  correlation peak between  $\gamma$ -ray and radio indicates that the  $\gamma$ -ray emission region is located  $5.02 \pm 0.46$  pc in the up stream of the 15 GHz radio core region, which is most probably beyond the BLR region.
- The variation of  $R - J$  indicates a bluer-when-brighter trend, while  $\delta V - \delta R$  shows no evident trend due to the sparse sample. We proposed the  $r$ -dependent spectral index model, i.e., emissions at different locations in the jet will contribute different spectral indices, to explain the spectral behaviors. This model is complementary for the shock in jet model, and manifests the opacity effects in the radiation process. The  $\gamma$ -ray spectral index decreases when the  $\gamma$ -ray flux increases, and approximates around a certain value at highest fluxes. Further work is needed to study the time bin effects on spectral fitting of  $\gamma$ -ray.
- We proposed to calculate the core-shift offsets, the magnetic field and lepton number density by time lags at different wavelengths. This method is an alternative for the core-shift measurements, can overcome the low spatial resolution difficulty in optical and  $\gamma$ -ray observations by using time series. The derived core-shift offset and magnetic fields agree well with that derived from the VLBI radio images. Also, the derived number densities consistently reproduces the observed maximal flux at  $R$  band for our target.

In the last, PMN J2345-1555 has a very compact jet, which is an interesting target for AGN jet property studies via multiple frequency observations.

This work has been funded by the National Natural Science Foundation of China under Grant No. U1531105, 11403015 and 11873035, the Natural Science Foundation of Shandong Province under Grant No. ZR2014AQ007, ZR2017PA009 and JQ201702, also partly by Young Scholars Program of Shandong University, Weihai (No. 20820162003). Data from the Steward Observatory spectropolarimetric monitoring project were used. This program is supported by Fermi Guest Investigator grants NNX08AW56G, NNX09AU10G, NNX12AO93G, and NNX15AU81G. This paper has made use of up-to-date SMARTS optical/near-infrared light curves that are available at [www.astro.yale.edu/smarts/glast/home.php](http://www.astro.yale.edu/smarts/glast/home.php). This research has made use of data from the OVRO 40-m monitoring program (Richards, J. L. et al. 2011, ApJS, 194, 29) which is supported in part by NASA grants NNX08AW31G, NNX11A043G, and NNX14AQ89G and NSF grants AST-0808050 and AST-1109911.

*Facilities:* Fermi(LAT), Steward, SMARTS, OVRO:40m

## REFERENCES

- |  |   |
|--|---|
| <p>Acero, F., et al., 2015, ApJS, 218, 23<br/> Achterberg, A., et al., 2001, MNRAS, 328, 393<br/> Ackermann, M., et al., 2015, ApJ, 813, L41<br/> Algaba, J. C., et al. 2018, ApJ, 852, 30<br/> Atwood, W. B., Abdo, A. A., Ackermann, M., et al. 2009, ApJ, 697, 1071<br/> Britto, R.J. et al., 2016, ApJ, 830, 162<br/> Bonning, E., et al., 2012, ApJ, 756, 13<br/> Chatterjee et al., 2012, ApJ, 749, 191<br/> Cohen M. H., Lister M. L., Homan D. C., et al., 2007, ApJ, 658, 232</p> | <p>Edelson, R. A. &amp; Krolik, J. H. 1988, ApJ, 333, 649<br/> Fuhrmann, L., Larsson, S., Chiang, J. et al, 2014, MNRAS, 441, 1899<br/> Fuhrmann, L., Angelakis, E., Zensus, J.A. et al., 2016, A&amp;A, 596, 45<br/> Ghisellini, G. and Tavecchio, F. and Foschini, L., Bonnoli, G. Tagliaferri, G., 2013, MNRAS, 432, L66-70<br/> Guo, F., Liu, Y. H., Daughton, W. and Li, H., 2015, ApJ, 806, 167<br/> Hirotani, K., 2005, ApJ, 619, 73</p> |
|--|---|

- Hovatta T., Valtaoja E., Tornikoski M., Lähteenmäki A., 2009, *A&A*, 494, 527
- Hodgson, J.A., Krichbaum, T. P., Marscher, A.P., et al., 2017, *A&A*, 597, 80
- Ikejiri, Y., Uemura, M., Sasada, M., et al. 2011, *PASJ*, 63, 639
- Jackson, N. & Browne, I. W. A., 1991, *MNRAS*, 250, 414-421
- Kang, S. J., Chen, L., & Wu Q. W., 2014, *ApJS*, 215, 5
- Kiehlmann, S., Savolainen, T., Jorstad, S.G., et al., 2016, *A&A*, 590, A10
- Kirk, J.G., Rieger, F.M., and Mastichiadis A., 1998, *A&A*, 333, 452-458
- Konigl A., *ApJ*, 1981, 619, 73
- Kudryavtseva, N. A., Gabuzda, D.C., Aller, M.F., Aller, H.D., 2011, *MNRAS*, 415, 1631
- Lasson, S., 2012, *arxiv:1207.1459v1*
- Lico, R., Giroletti, M., Gomez, J. L., et al., 2014, *A&A*, 571, A54
- Lister M. L., et al., 2009, *AJ*, 137, 3718
- Lister M. L., et al., 2016, *ApJ*, 152, 12
- Lobanov, A.P. 1998, *A&A*, 330, 79
- Marscher, A. P., Jorstad, S. G., D'Arcangelo, F. D., et al. 2008, *Nature*, 452, 966
- Max-Moerbeck W. et al., 2014a, *MNRAS*, 445, 428-436
- Max-Moerbeck W. et al., 2014b, *MNRAS*, 445, 437-459
- O'Sullivan S.P., & Gabuzda D.C., 2009, *MNRAS*, 400, 26-42
- Peterson, B. M., et al., 1998, *PASP*, 110, 660-670
- Potter, W. J. & Cotter G., 2012, *MNRAS*, 423, 756-765
- Pushkarev, A.B., Kovalev, Y.Y., Lister, M. L., and Savolainen, 2009, *A&A*, L33-L36
- Pushkarev, A.B., Kovalev, Y.Y., and Lister, M. L., 2010, *ApJ*, 722, L7-L11
- Pushkarev, A. B. et al., 2012, *A&A*, 545, 113
- Richards, J. L. et al, 2011, *ApJS*, 194, 29
- Sari, R., Piran, T., Narayan, R., 1998, *ApJ*, 497, L17-L20
- Smith, P.S., et al., 2009, *arXiv:0912.3621*, 2009 Fermi Symposium, eConf Proceedings C091122.
- Tachibana, Y., and Kawai, N. 2015, *arXiv:1502.03610v1*
- Timmer, J., & Koenig M., 1995, *A&A*, 300, 707
- Schmidt, G.D., Stockman, H.S., & Smith, P.S. 1992, *ApJ*, 398, L57
- Villata, M., et al., 2006, *A&A*, 453, 817-822
- Welsh, W. F., 1999, *PASP*, 111, 1347
- Wu, L. H., Wu Q. W., Yan, D. H., Chen, L. & Fan, X. L., 2018, *ApJ*, 852, 45
- Yan D.H., Wu, Q.W., Fan, X. L., Wang, J.C. & Zhang, L., 2018, *ApJ*, 859, 168
- Zamanimasab M., et al., 2014, *Nature*, 510, 126

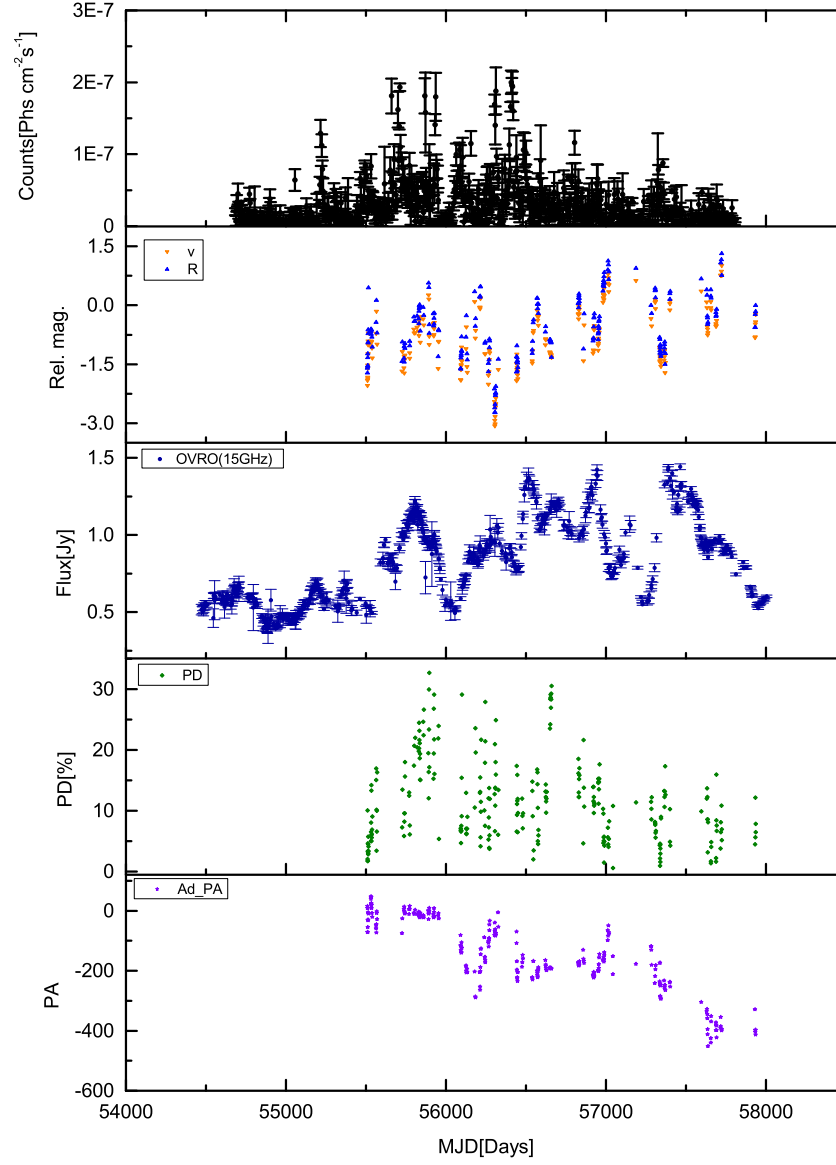


**Figure 1.** The light curves of  $0.3 \rightarrow 0.9$  GeV  $\gamma$ -ray, optical V and R (relative magnitudes), radio 15 GHz, polarization degree and adjusted polarization angle are plotted from up to bottom panels.

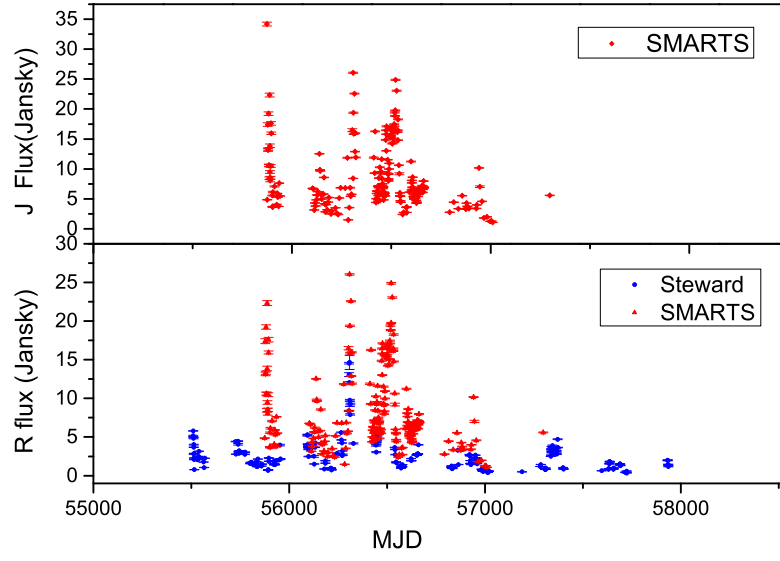


**Figure 2.** The calibrated J and R fluxes are presented in the top and bottom panels, respectively.

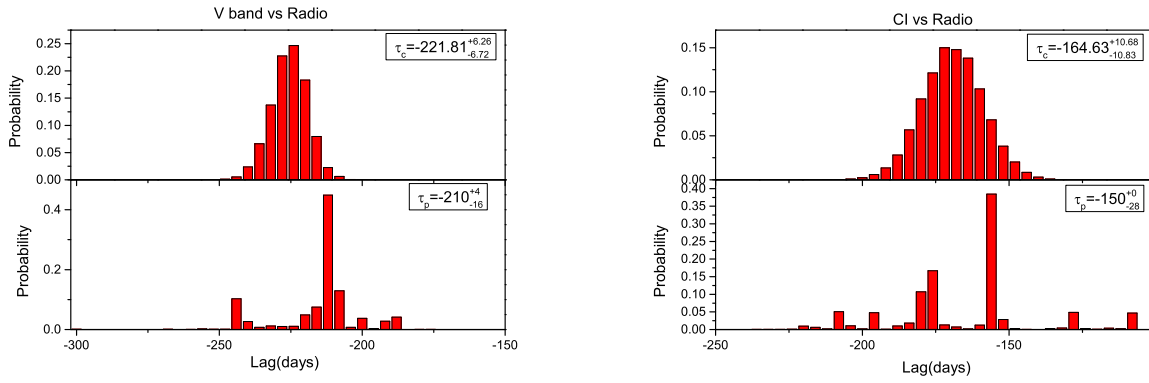


**Figure 3.** The histogram of the centroid and peak lag times are plotted. The left two panels show the probability distribution of FR/RSS MC at different lag times for the optical V band against the radio. The right two panels show that for the color index against the radio. The upper and lower errors in  $\tau_c$  and  $\tau_p$  are the limits of  $1\sigma$  range.

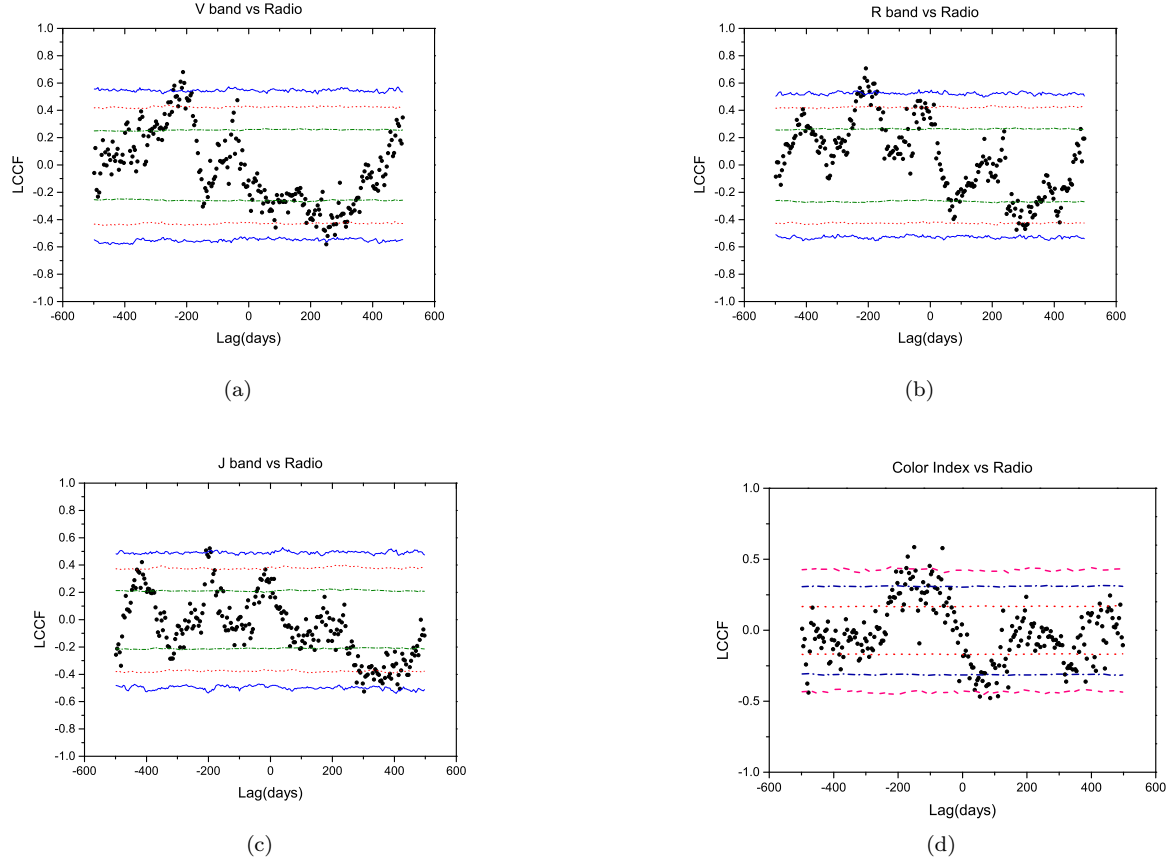


**Figure 4.** The LCCFs of optical  $V$ ,  $R$ ,  $J$  band and  $\delta V - \delta R$  CI versus 15 GHz radio light curves are plotted in a, b, c and d panels, respectively. The correlation significance are indicated by the olive dash dot ( $1\sigma$ ), red dot ( $2\sigma$ ) and blue solid ( $3\sigma$ ) lines, respectively. The positive value of lag time indicates the former lags behind the latter.

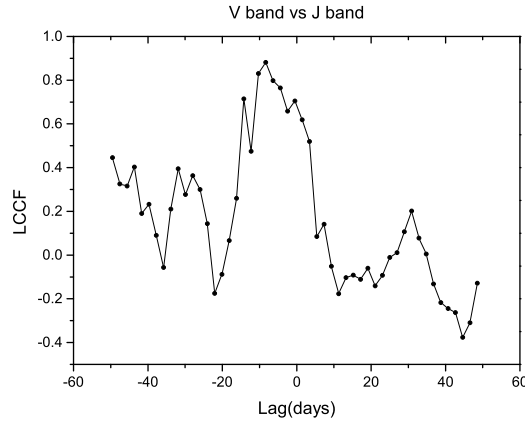


**Figure 5.** The LCCF between the  $V$  band and the  $J$  band is plotted.

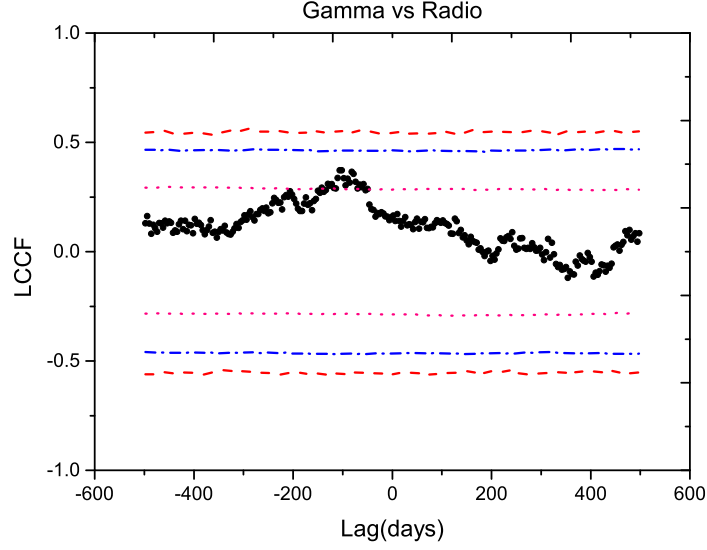


**Figure 6.** The LCCF calculation of  $\gamma$ -ray and 15 GHz radio are represented.

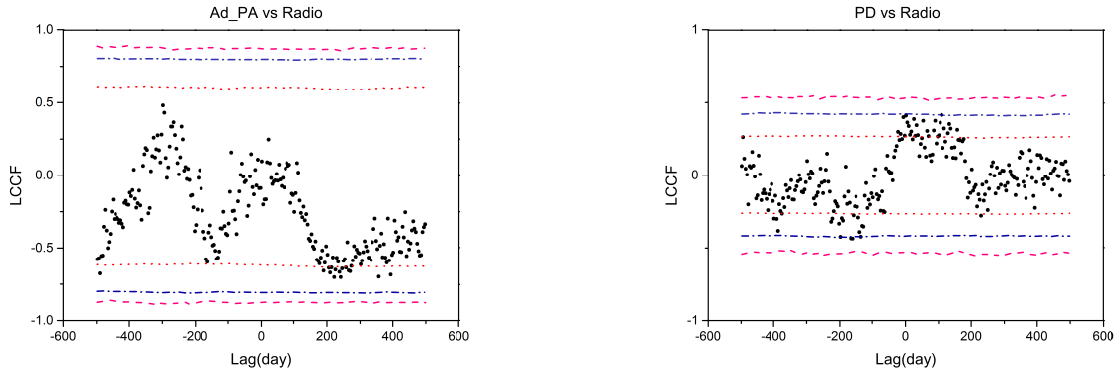


**Figure 7.** The LCCFs of adjusted PA and PD versus radio are plotted in the left and right panel, respectively.

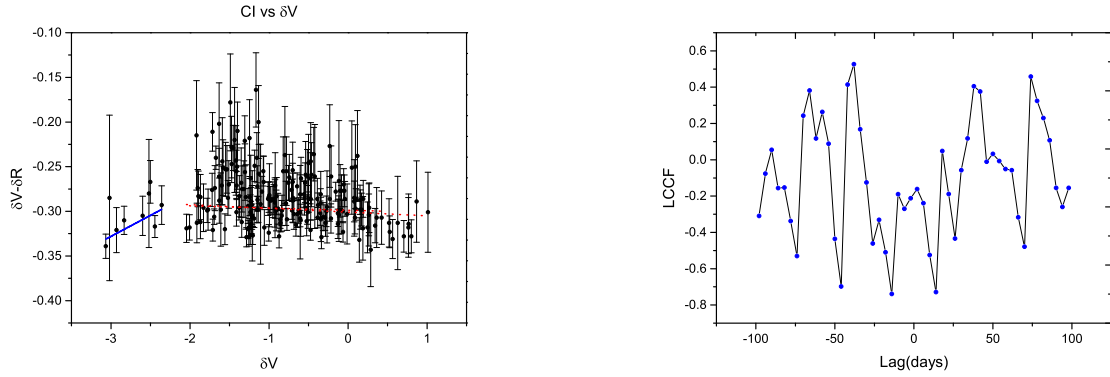


**Figure 8.** The  $\delta V - \delta R$  versus the  $\delta V$  is plotted in the left panel, and the LCCF between the  $\delta V - \delta R$  and  $\delta V$  is plotted in the right panel. In the left panel, the linear fitting analysis  $y = a + bx$  is applied to two ranges of  $\delta V$ . The blue solid line denotes the fitting results for the range  $\delta V < -2$ , while the red dash line denotes that of  $\delta V > -2$ . The slope  $b$  and the Pearson's  $r$  value for the blue and red lines are (0.047, 0.642) and (-0.004, -0.107), respectively.

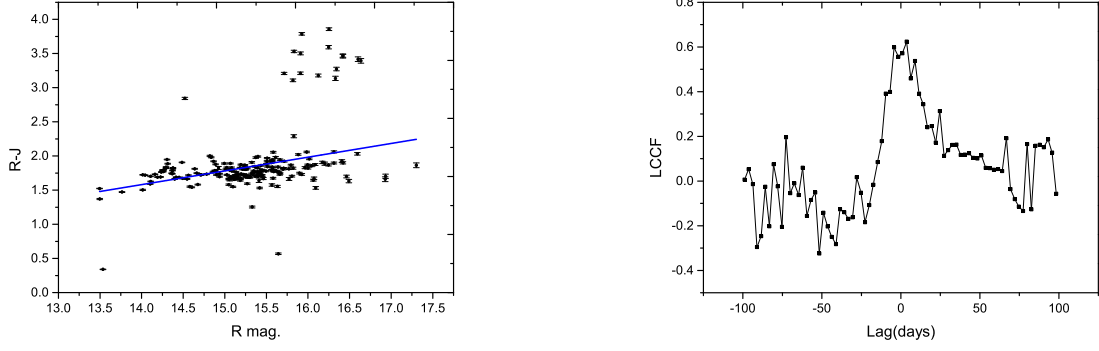


**Figure 9.** The  $R-J$  versus  $R$  magnitude and the LCCF between them are plotted in the left and right panel, respectively. The (b,r) of the blue solid line in the left panel is (0.201, 0.433). The peak in the right panel has a correlation value 0.624.

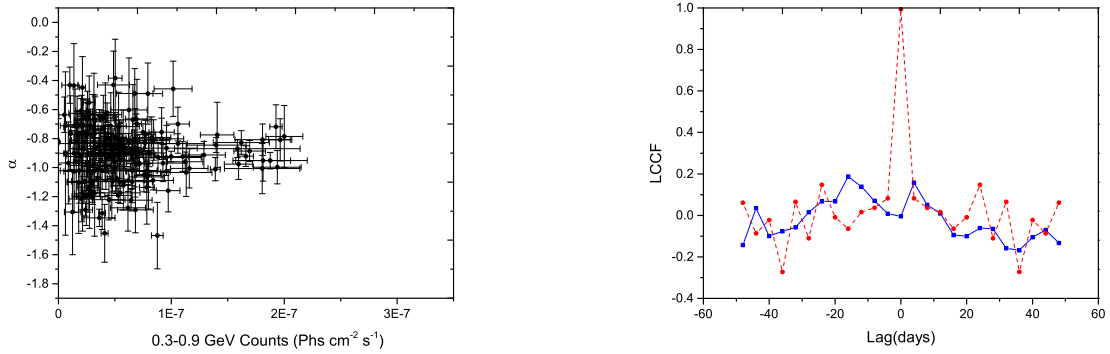


**Figure 10.** The  $\gamma$ -ray spectral indices versus **b** band  $\gamma$ -ray flux is plotted in the left panel. In the right panel, the LCCF of between **b** band fluxes and spectral indices is marked with the blue square solid line, while the LCCF of  $\gamma$ -ray spectral index is marked with the red circle dash line. Note that the peak of the blue solid line corresponds to the valley of the red dash line.

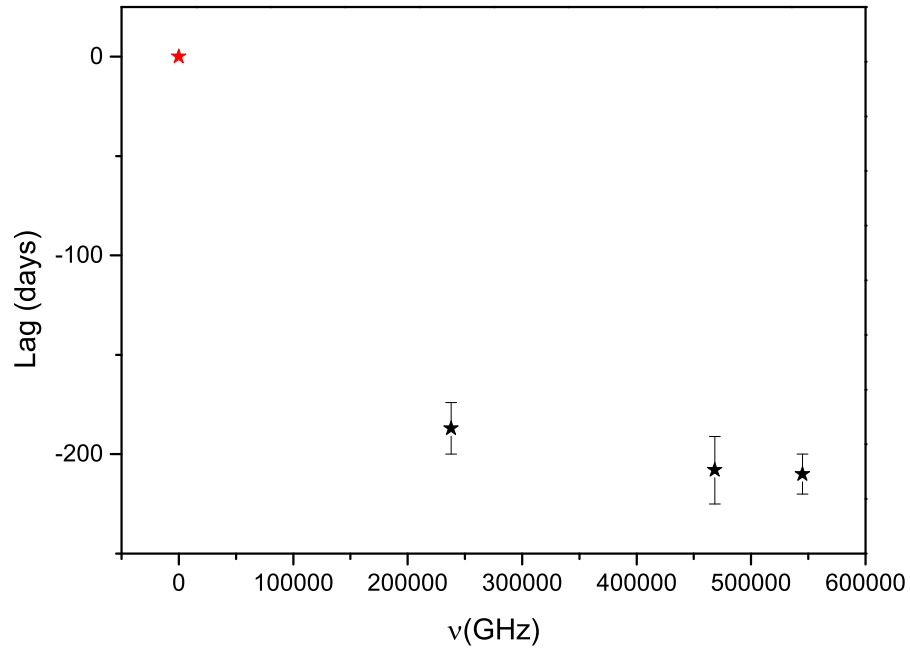


**Figure 11.** Lag days ( $\tau_c$ ) between  $V$ ,  $R$ ,  $J$  and 15 GHz radio are plotted.

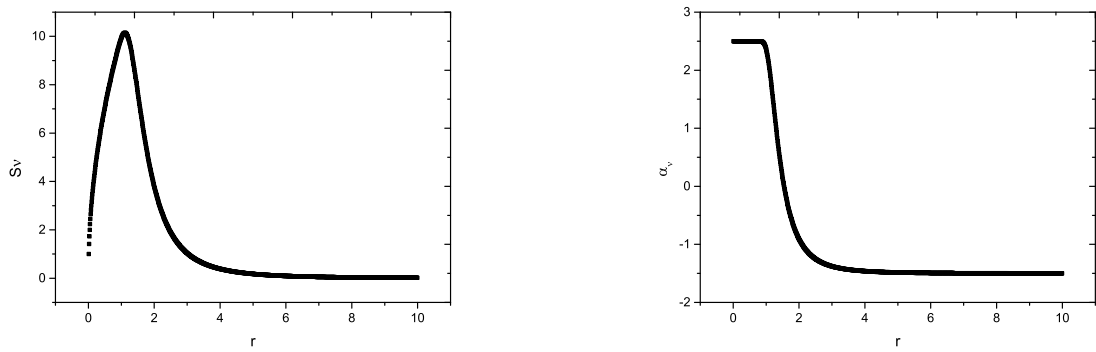


**Figure 12.** The flux  $S_\nu$  and the spectral index  $\alpha_\nu$  as functions of  $r$  are plotted numerically in the left and right panel, respectively. The units of  $S_\nu$  is taken arbitrarily.